International Journal of Rock Mechanics & Mining Sciences 171 (2023) 105576

Contents lists available at ScienceDirect

International Journal of Rock Mechanics and Mining Sciences

journal homepage: www.elsevier.com/locate/ijrmms

Bi-modular properties of sandstone inferred from seismic moment tensors of acoustic emissions

Václav Vavryčuk [a,b,*], Matěj Petružálek [b], Tomáš Lokajíček [b], Ali Aminzadeh [b]

[a] Institute of Geophysics of the Czech Academy of Sciences, Prague, Czech Republic
[b] Institute of Geology of the Czech Academy of Sciences, Prague, Czech Republic

ARTICLE INFO

Keywords:
Acoustic emissions
Tensile cracks
Rock
Auxetic behaviour
Fracturing
Rock bi-modularity

ABSTRACT

We propose a novel method for studying the λ/μ ratio, the v_P/v_S ratio and Poisson's ratio of rocks based on the determination of highly accurate moment tensors of acoustic emissions (AEs). The validity of the method is verified on observations of 539 AEs recorded in a sandstone sample during a semi-circular bend test. We show that the sandstone exhibits the so-called bi-modular behaviour indicating that rock parameters significantly differ under compressive and tensile stress regimes. In addition, the zone characterized by highly tensile fractures is auxetic. For increasing shear component in AEs, Poisson's ratio increases and the auxetic effects disappear. The proposed approach for determining the λ/μ, v_P/v_S, and Poisson's ratios using AEs is fully independent of standard techniques based on measuring deformation of rock samples. The approach might find applications in detailed studies of rock behaviour under various stress conditions, in particular, in assessing the bi-modularity of rocks measured during a single experiment.

1. Introduction

The seismic moment tensor (MT) describes equivalent body forces acting at a source of seismic or seismo-acoustic waves.[1] It is a basic quantity characterizing a fracture process in the focal zone on all scales: from earthquakes in the field to acoustic emissions in the lab. The MTs can be decomposed into double-couple (DC), isotropic (ISO), and compensated linear vector dipole (CLVD) components.[2,3] The DC component informs us about the orientation of the activated fracture and direction of the shear slip along the fracture. The ISO and CLVD components reflect complexities in fracturing, seismic anisotropy in the fracture zone, or its volumetric changes such as inflation or deflation of magma chambers in volcanic areas, processes associated with rock bursts in mines, and collapses of structures with cavities or pores.[4–12]

A common mechanism producing the ISO and CLVD components is shear-tensile fracturing where fractures, cracks or microcracks can possibly open or close during the rupture process.[13–18] This phenomenon is observed in areas with tensile tectonics,[19] in geothermal and volcanic areas characterized by high fluid pressure[12,20–22] or in laboratory experiments with acoustic emissions (AEs), which involve tensile stress, such as the Brazilian splitting tests.[23] Tensile motions can also occur during shear rupturing when tensile wing cracks develop at the tip of the fracture.[24–26]

The shear-tensile source model (Fig. 1) is a general dislocation model described by three angles (strike, dip, and rake) defining geometry of shear faulting/fracturing and another angle (slope) defining how tensile the source is. Additionally, the model is characterized by the v_P/v_S ratio (or equivalently by the ratio of the Lamé coefficients λ/μ or the Poisson's ratio ν), which refers to properties of the material in the focal area. Both the slope angle and the v_P/v_S ratio in the focal area are important parameters calculated from MTs that can improve our understanding of the fracture process. In contrast to the v_P/v_S ratio calculated from measurements of P- and S-wave velocities in an unfractured medium, the ratio determined from MTs is often different. Since it is usually significantly lower than the standard value specified for intact rock, it is argued that this value is local and reflects properties of fractures. It has also been revealed that this ratio is quite sensitive to processes in the focal zone and it can vary over time.[16]

We know from various experiments that the mechanical properties are different in the focal zone than in intact rock because the increase of porosity and opening of microcracks is forced in this zone, in particular, under the tensile stress regime. This results in distinctly different behaviour of rocks observed in tensile and compressive modes.[27] This behaviour is called bi-modular, and it can be assessed by measuring the

* Corresponding author. Institute of Geophysics of the Czech Academy of Sciences, Boční II 1401, 14100 Prague, Czech Republic.
E-mail address: vv@ig.cas.cz (V. Vavryčuk).

https://doi.org/10.1016/j.ijrmms.2023.105576
Received 29 December 2022; Received in revised form 31 July 2023; Accepted 4 September 2023
Available online 14 September 2023
1365-1609/

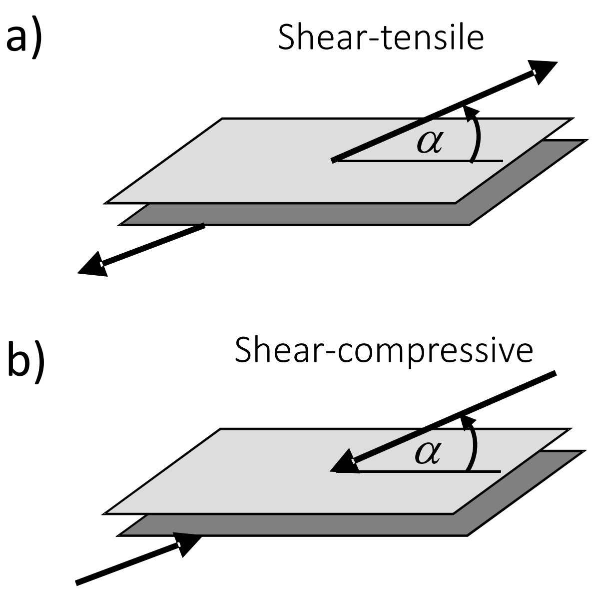

Fig. 1. Scheme of the shear-tensile and shear-compressive events. Angle α is the slope angle which quantifies the non-shear component of the focal mechanism; angle α is positive for tensile events but negative for compressive events. For shear events, angle α is zero.

strength and the Poisson's ratio of rocks subjected to uniaxial compression and Brazilian tensile testing. The measurements consistently show significantly lower strength and Poisson's ratio in tension compared to compression for rocks such as sandstone, marble, granite or basalt.[28–32] Lowering the Poisson's ratio under effective tensile stresses in quartz-rich sandstone can even lead to auxetic effects, where the Poisson's ratio becomes negative, as reported by Li and Ji.[33] Since the mechanical properties in the focal zone inferred using MTs are highly sensitive to local conditions in the fractured zone, the analysis of MTs of AEs could potentially contribute to the study of rock's bi-modularity.

In this paper, we focus on studying properties of shear-tensile fracturing determined from highly accurate MTs of acoustic emissions recorded in a sandstone sample during the semi-circular bend test. Specifically, we investigate the λ/μ ratio, the v_P/v_S ratio, and the Poisson's ratio as a function of the tensile character of fracturing. Our findings show that the mechanical properties of fractures are sensitive to the slope angle implying that the shear and tensile fractures behave differently. This is a clear indication of the bi-modular behaviour of fractured rocks. We discuss a possible physical origin of this phenomenon and its significance for understanding fracture processes in rocks. We demonstrate that the proposed method is unique because it is capable of measuring rock properties for a mixed stress mode and studying the bi-modularity of rocks within a single experiment.

2. Theory

2.1. Seismic moment tensor for the shear-tensile dislocation model

Moment tensor $\mathbf{M}$ of the shear-tensile source (Fig. 1) in isotropic rocks is expressed as[13,14]

$$M_{ij} = uS\left[\lambda N_k n_k \delta_{ij} + \mu\left(N_i n_j + N_j n_i\right)\right], \tag{1}$$

where u is the slip, S is the fracture area, λ and μ are the Lamé's coefficients, and n_i and N_i are the unit vectors defining the normal to the fracture and the slip direction, respectively.

The fracture normal $\mathbf{n}$ and the dislocation direction $\mathbf{N}$ are expressed for the tensile source in terms of angles φ, δ, θ and α as follows[14]:

$$\begin{aligned} n_1 &= -\sin\delta\sin\varphi, \\ n_2 &= \sin\delta\cos\varphi, \\ n_3 &= -\cos\delta, \end{aligned} \tag{2}$$

$$\begin{aligned} N_1 &= (\cos\theta\cos\varphi + \cos\delta\sin\theta\sin\varphi)\cos\alpha - \sin\delta\sin\varphi\sin\alpha, \\ N_2 &= (\cos\theta\sin\varphi - \cos\delta\sin\theta\cos\varphi)\cos\alpha + \sin\delta\cos\varphi\sin\alpha, \\ N_3 &= -\sin\theta\sin\delta\cos\alpha - \cos\delta\sin\alpha. \end{aligned} \tag{3}$$

Angles φ, δ, θ and α are called the strike, dip, rake and slope, respectively. These angles are, in general, functions of spatial coordinates and time. For simplicity, we adopt a point source approximation of tensile fracturing on a planar fracture and assume these angles constant for each source.

2.2. Inversion for the moment tensor

The moment tensor inversion for one individual seismic source is based on the following equation[34,35]:

$$\mathbf{Gm} = \mathbf{u}, \tag{4}$$

where $\mathbf{G}$ is the Kx6 matrix of the spatial derivatives of the Green's function, which describes a dynamic response of the rock to applied dipole forces in the source for K sensors. Vector $\mathbf{m}$ is composed of 6 components of the moment tensor $\mathbf{M}$,

$$\mathbf{m} = [M_{11}, M_{22}, M_{33}, M_{23}, M_{13}, M_{12}]^T, \tag{5}$$

and $\mathbf{u}$ is the vector of maximum displacement amplitudes of direct waves or of full displacement waveforms observed at K sensors.

The moment tensor $\mathbf{M}$ is obtained by inverting Eq. (4) using the generalized least-squares inversion. In order the inverted MTs to be well constrained, it is desirable to employ a large number of sensors K. Since the MT inversion is linear, it is fast and computationally undemanding. In addition, the MT inversion can produce the source-time function, provided the whole waveforms instead of the amplitudes of waves are inverted.

2.3. Properties of fractures derived from moment tensors

The slope angle α defining the deviation of the slip from the fracture plane (see Fig. 1) is calculated from the moment tensor $\mathbf{M}$ as[14]

$$\sin\alpha = \frac{M_1 + M_3 - 2M_2}{M_1 - M_3}, \tag{6}$$

where the eigenvalues of $\mathbf{M}$ are denoted as $M_1 \geq M_2 \geq M_3$. The λ/μ and the v_P/v_S ratios are calculated as[14]

$$\frac{\lambda}{\mu} = \frac{2M_2}{M_1 + M_3 - 2M_2}, \quad \frac{v_P}{v_S} = \sqrt{2\frac{M_1 + M_3 - M_2}{M_1 + M_3 - 2M_2}}, \tag{7}$$

or in terms of the percentages of the ISO and CLVD components as

$$\frac{\lambda}{\mu} = \frac{4}{3}\left(\frac{\mathrm{ISO}}{\mathrm{CLVD}} - \frac{1}{2}\right), \quad \frac{v_P}{v_S} = \sqrt{\frac{4}{3}\left(\frac{\mathrm{ISO}}{\mathrm{CLVD}} + 1\right)}. \tag{8}$$

Taking into account the following equations for the Poisson's ratio ν

$$\nu = 0.5\left(1 - \frac{1}{(v_P/v_S)^2 - 1}\right) \text{ and } \nu = 0.5\frac{\lambda/\mu}{\lambda/\mu + 1}, \tag{9}$$

we get

$$\nu = \frac{M_2}{M_1 + M_3} = \frac{\left(2\frac{\mathrm{ISO}}{\mathrm{CLVD}} - 1\right)}{\left(4\frac{\mathrm{ISO}}{\mathrm{CLVD}} + 1\right)}. \tag{10}$$

The ISO and CLVD percentages are obtained from the decomposition of MTs into the DC and non-DC MT components[3]

$$\mathrm{ISO} = \frac{M_{\mathrm{ISO}}}{M}, \quad \mathrm{CLVD} = \frac{M_{\mathrm{CLVD}}}{M}, \quad \mathrm{DC} = \frac{M_{\mathrm{DC}}}{M}, \tag{11}$$

where

$$M_{\mathrm{ISO}} = \frac{1}{3}(M_1 + M_2 + M_3),$$
$$M_{\mathrm{CLVD}} = \frac{2}{3}(M_1 + M_3 - 2M_2), \tag{12}$$
$$M_{\mathrm{DC}} = \frac{1}{2}(M_1 - M_3 - |M_1 + M_3 - 2M_2|),$$

and

$$M = |M_{\mathrm{ISO}}| + |M_{\mathrm{CLVD}}| + M_{\mathrm{DC}}. \tag{13}$$

The sum of the absolute values of the DC, CLVD and ISO percentages is 100%.

3. Data

3.1. Experimental setup and tested rock

The acoustic emission (AE) data were recorded during the semi-circular bend test used for obtaining the fracture toughness.[36] An intact Tesin sandstone from the Reka mine (Czech Republic) was the tested rock. It was a fine-grained (grain size <0.25 mm) compact sandstone with density of 2500 kg/m^3 and open porosity of 5%. The rock was transversely isotropic (TI), with the symmetry axis along the z-axis being perpendicular to its bedding (Fig. 2). The seismic velocities obtained from ultrasonic sounding are as follows: (1) the P velocities in the symmetry plane and along the symmetry axis are $v_P = 4.1$ km/s and $v_{PZ} = 3.34$ km/s, respectively; (2) the SH and SV velocities in the symmetry plane are $v_{SH} = 2.61$ km/s and $v_{SV} = 2.39$ km/s, respectively. The polarization of the SH wave lies in the symmetry plane, the polarization of the SV wave is perpendicular to the symmetry plane.

To circumvent the effects of anisotropy in a transversely isotropic rock, the bedding was parallel to the xy-plane and perpendicular to the z-axis of the specimen, which is called the divider in the literature.[37,38] The dimensions of the semi-circular specimen are specified in Fig. 2a. The supports positions were symmetric around the notch. This test design follows the ISRM suggested method,[36] and should result in tension loading at the tip of the crack. The tension failure in a highly damaged region at the tip of the crack, called the fracture process zone (FPZ), is expected as well. The servo-controlled loading frame (MTS 815, USA) was controlled by the vertical displacement feedback with a constant increment of 0.005 mm/min.

3.2. Data acquisition system and loading of the rock

AEs were recorded by 22 sensors (Fuji AE204A) attached to the specimen (Fig. 2a). Sensors were 8 mm in diameter, had a reasonably flat frequency characteristics within the range of 240–520 kHz, and with a particle velocity sensitivity of 708 V/m/s. AE waveforms were recorded by a multi-channel, transient recorder (Vallen System AMSY6, Germany). The apparatus was set up in a triggered regime (40 dB threshold). The sampling rate was 10 MHz, and the length of the recorded waveforms was 1024 points with 256 points of the pre-triggering sequence. Each point was recorded with a 16-bit resolution.

The specimen failed according to the expectations: the tensile macrocrack started to develop at the tip of the notch, and propagated in the vertical (y-axis) direction without any significant kinking (Fig. 2b). The maximum axial load was reached at 3.16 kN, resulting in the fracture toughness of 1.25 MPa$\sqrt{\mathrm{m}}$ based on the reference plots presented in Nejati et al.[39] However, if the crack kinks from the vertical line, the fracture toughness should be corrected as described in Nejati et al.[40] The AE activity started at 70% of the maximum load, then it slightly increased up to 95%, where a sharp exponential increase led to the failure of the specimen.

4. Results

4.1. Basic characteristics of the AE dataset

About 1500 AEs were recorded in total. First arrival times and amplitudes were measured by a two-step Akaike's information criterion (AIC) picker.[41] A grid search method[42] was used for locating the AEs (Fig. 3). The accuracy of AE locations is within 2 mm. This value was verified by locating events generated by a pencil lead breakage performed above the notch position before running the test. To prepare a homogenous AE data set, we imposed the following criteria for selecting AEs. We considered AEs: (1) with at least 20 reliable first arrival times and amplitude picks; (2) located in the fracture zone surrounding the crack tip; and (3) occurring within the range of 95–100% of the maximum loading force. In this way, we selected 982 AEs suitable for a reliable retrieval of seismic moment tensors. The peak-to-peak first arrival amplitudes, corrected for the influence of a directional sensitivity of the AE sensors served as an input for the network calibration[43,44] and for the MT inversion (for more details, see Petružálek et al.[18]).

Figs. 3 and 4 display the AE events selected for the further MT analysis. They occurred in the interval of 95–100% of the maximum stress, just before the brittle stress drop that coincided with the propagation of the macro-fracture from the FPZ to the top of the loaded specimen. Based on the AE locations, the parameters of the FPZ were

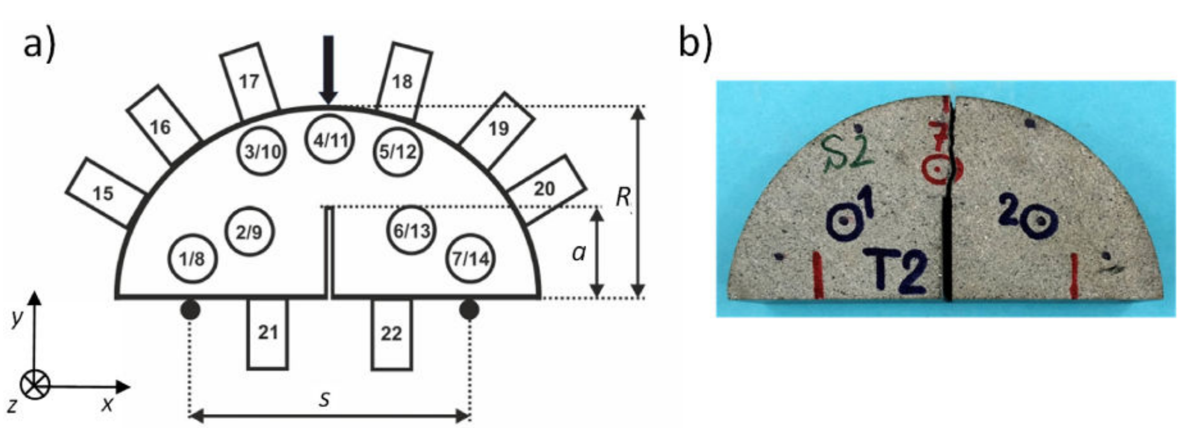

Fig. 2. a) Sketch of 22 AE sensor's positions and geometry of the tested specimen: radius of the sample $R = 46.6$ mm; thickness of the sample $w = 33.5$ mm, span of supports positions $s = 56$ mm; and the length of the notch $a = 23.3$ mm and its thickness was 1 mm. The bedding plane of the sandstone (symmetry plane of TI) was parallel to the xy-plane. The symmetry axis of TI is parallel to the z-axis. b) A photo of the fractured specimen after the test.

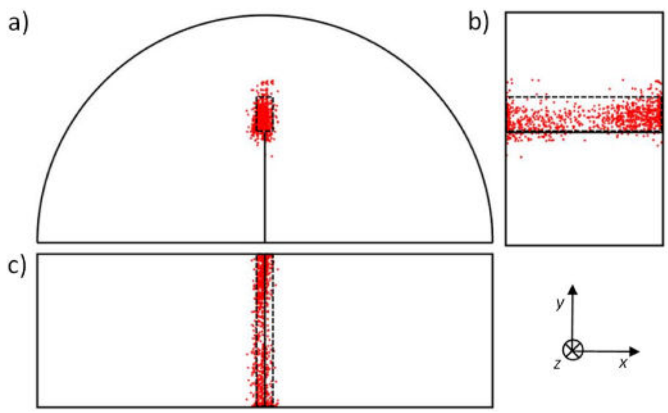

Fig. 3. Locations of the selected 982 AEs with the estimation of the size of the fracture process zone (FPS): length ~ 7 mm; diameter ~ 3 mm. a) Projections onto the *xy*-plane (a), *zy*-plane (b), and *xz*-plane (c).

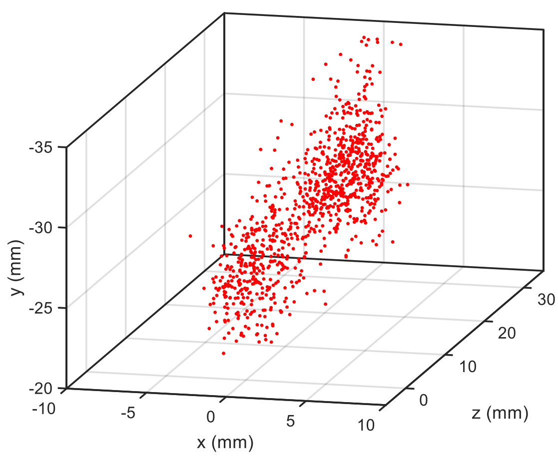

Fig. 4. 3D plot of locations of the selected 982 AEs – a close up view. For an animation of rotating 3D locations of AEs, see the Supplementary video.

estimated: length ~7 mm; diameter ~3 mm. The FPZ is symmetric along the notch, without any sign of kinking at the tip. It developed rather homogeneously throughout its volume with a slightly higher density of AEs near the surfaces. Considering the grain size of ~0.25 mm, the measured size of the FPZ is reasonable. Similar results were reported in Lin et al.[45] for the Berea sandstone.

4.2. MT inversion of AEs

The MT inversion of AEs is not an easy task, because the recorded AEs are influenced by many complex phenomena, such as high-frequency noise, waveform attenuation and scattering, seismic anisotropy of the rock sample, and coupling effects between sensors and the sample. Furthermore, the MT inversion is a data-demanding procedure, requiring accurate locations of seismic (or seismo-acoustic) sources, an accurate velocity model, and dense sensor coverage on the focal sphere.[15,23,46] We can invert amplitudes of seismic phases, amplitude ratios or full waveforms.[47–50] The suitability of individual MT inversions is specific, depending on the predominant wave frequencies and the complexity of waveforms.

In our study, MTs of AEs observed during the experiment were calculated using amplitudes of direct P waves recorded at least at 20 sensors calibrated using the network calibration method.[43,44] Such inversion is advantageous for several reasons: (1) P-wave amplitudes are less sensitive to small-scale complexities and seismic anisotropy in rocks compared to S-wave amplitudes or full waveforms.[51–53] (2) A high number of sensors with excellent focal sphere coverage ensures that the inversion problem is well constrained and errors due to mismodelling are minimized. (3) The calibration procedure suppresses systematic unmodelled effects of waveform attenuation and coupling effects between sensors and the sample.[23,54]

4.3. Selection of highly accurate MTs

We calculated MTs of all 982 AEs, locations of which are shown in Fig. 3 (for the complete list of MTs, see the Supplement). The quality of MTs was assessed by calculating the normalized root-mean-square (RMS) difference between theoretical and observed amplitudes A_i^{synth} and A_i^{obs}

$$\mathrm{RMS} = \frac{\sqrt{\sum_{i=1}^{K}\left(A_i^{synth} - A_i^{obs}\right)^2}}{\sqrt{\sum_{i=1}^{K}\left(A_i^{synth}\right)^2}}, \tag{14}$$

where i is the sequential number of a sensor, and K is the total number of sensors. The MTs are normalized to their maximum eigenvalue. The MTs were decomposed into the DC, CLVD, and ISO components using Eqs 11–13. The mean errors of the components were calculated as the standard deviations of values obtained by a repeating MT inversion with data contaminated by random noise. The probability distribution of noise was flat, the noise level was up to 25% of the maximum P-wave amplitude at each sensor, and the number of noise realizations was 100.

Since the non-DC components of MTs are particularly sensitive to errors produced by the MT inversion, we analysed only the most accurate MTs. Hence, we selected 539 most accurate MTs based on the following selection criteria: (1) The normalized root-mean-square (RMS) difference between theoretical and observed amplitudes calculated by Eq. (14) was lower than 0.35, and (2) the standard deviation of the ISO and CLVD percentages was lower than 3% and 6%, respectively. In this way, we obtained a dataset of highly accurate MTs, which was sufficiently large for further statistical analyses.

4.4. Non-DC components of MTs

The focal mechanisms of the selected 539 AEs are well-clustered as seen in the composite figure of the pressure/tension (P/T) axes on the focal sphere (Fig. 5, inset). As expected, the T-axes are close to the *x*-axis,

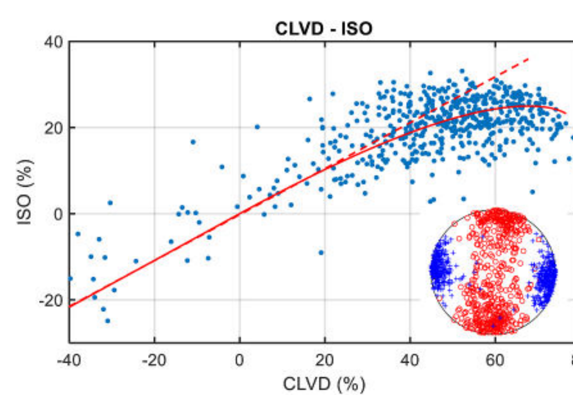

Fig. 5. The CLVD-ISO plot of the analysed 539 AE events. Inset: the P-axes (red circles) and T-axes (blue plus signs) on the focal sphere. The full red curve shows the optimum CLVD-ISO function derived from a linearly dependent v_P/v_S ratio, see Fig. 6b. The dashed red straight line shows the theoretical CLVD-ISO function for a constant v_P/v_S ratio. For details, see the text. (For interpretation of the references to colour in this figure legend, the reader is referred to the Web version of this article.)

which coincides with the direction of the maximum tensile stress (perpendicular to the notch). The P-axes lie in the y-z plane with the highest density along the y-axis. This direction corresponds to the maximum compression in the rock sample. The MTs are mostly tensile: 486 AEs display positive ISO and CLVD with the DC percentage lower than 75%. Only 22 AEs exhibit compressive MTs with negative ISO and CLVD and with a DC percentage lower than 75%. The remaining AEs show MTs with a shear character or MTs with a reverse sign of the ISO and CLVD.

Fig. 5 shows the dependence of the ISO and CLVD components of the 539 AEs. As seen in the figure, the values of individual AEs are rather scattered. This is due to the challenge of determining accurate non-DC components. The MT inversion is a data-demanding procedure, which is sensitive to noise in data and needs a detailed knowledge of the P velocity in the rock. Furthermore, the accuracy is influenced by the number and distribution of sensors on the focal sphere. Nevertheless, since we are analysing a large number of AEs, a systematic trend in the CLVD-ISO plot is visible for the whole dataset (Fig. 5, the full red line).

4.5. Non-linearity of the CLVD-ISO function

Surprisingly, the CLVD-ISO function is not linear in the whole range of the observed values, but it deviates from a straight line for highly tensile AEs with CLVD > 40% (compare the full and dashed red lines in Fig. 5). This phenomenon is unexpected and against the common assumption that the v_P/v_S ratio is constant for shear-tensile fractures in the same focal zone.[3] Nevertheless, the accuracy of the CLVD and ISO components in this study is high enough to exclude the possibility that the non-linearity of the CLVD-ISO function is an artefact of errors of the MT inversion. Hence, our data indicate that the assumption of a constant v_P/v_S ratio in the focal zone should be abandoned.

Finding that the v_P/v_S ratio determined from MTs is not constant in the focal region is surprising but not against existing observations. So far, the v_P/v_S ratio determined from MTs is mostly based on seismic data in focal zones characterized typically by compressive stress conditions.[14,19] The observed non-DC components of MTs of earthquakes are usually small. Focal mechanisms with significantly high tensile components are rather rare in seismic observations. As a result, there is a lack of statistically relevant seismic analyses regarding the v_P/v_S ratio in focal zones under tensile stress conditions. By contrast, exciting AEs with highly tensile mechanisms is quite common in lab experiments, where rocks are subjected to a tensile stress regime. However, the number and quality of MTs in such experiments are still not high enough to reveal details in the CLVD-ISO function.[23,55] From this perspective, the data shown in Fig. 5 are exceptionally accurate and worth detailed study.

4.6. Varying λ/μ ratio and v_P/v_S ratio

Fig. 6 shows the λ/μ ratio (a) and the v_P/v_S ratio (b) as a function of the slope angle for the 539 AEs. Similarly, as in Fig. 5, the data are rather scattered. The scatter is higher for shear AEs than for tensile AEs. For nearly shear AEs (the slope angle is very small), the denominators in Eq. (7) are close to zero, causing the λ/μ and v_P/v_S ratios to become unstable. This is because the λ/μ and v_P/v_S ratios cannot be determined for pure shear AEs. To reduce the scattering of individual measurements, the analysed data are binned. The bins are from 5° to 75°, with a bin width of 10°. The mean values in the bins are plotted together with the 99% confidence intervals and with the linear regression line (the blue dashed line). Fig. 6 illustrates that both the λ/μ and v_P/v_S ratios decrease with increasing slope angle. This points to a bi-modular behaviour of fractures, where shear fractures respond differently to stress in the rock compared to tensile fractures. Strikingly, the λ/μ ratio even becomes negative for slopes greater than 20–25°, reflecting an anomalously low value of the Lame's coefficient λ for tensile fracturing. For a detailed physical interpretation of this intriguing phenomenon, see the Discussion section.

5. Discussion

Cracks and fractures significantly influence physical properties of rocks, and understanding their effects is necessary for correctly interpreting geophysical data. From this perspective, studying the mechanical properties of fractured rocks using moment tensors of AEs is a promising approach with high potential. Since MTs are quite sensitive to the type of fracturing of AEs, they can discriminate between shear, compressive, and tensile fracture modes. Moreover, tensile fracturing is of particular interest because it increases the rock's porosity and it significantly reduces strength of the rock.

During the semi-circular bend test of the Tesin sandstone reported in this paper, a large number of tensile cracks with a preferential orientation subparallel to the notch was created. These cracks formed the FZP, characterized by considerably different (possibly anisotropic) properties of the rock. The prominent impact of tensile fracturing on rock properties is illustrated in Fig. 6. The figure shows the λ/μ ratio and the v_P/v_S ratio as a function of the slope angle α, which quantifies the degree of tensile character of AEs. Both quantities decrease with increasing angle α. Consequently, the Poisson's ratio ν defined in Eqs 9 and 10 should also decrease, see Fig. 7.

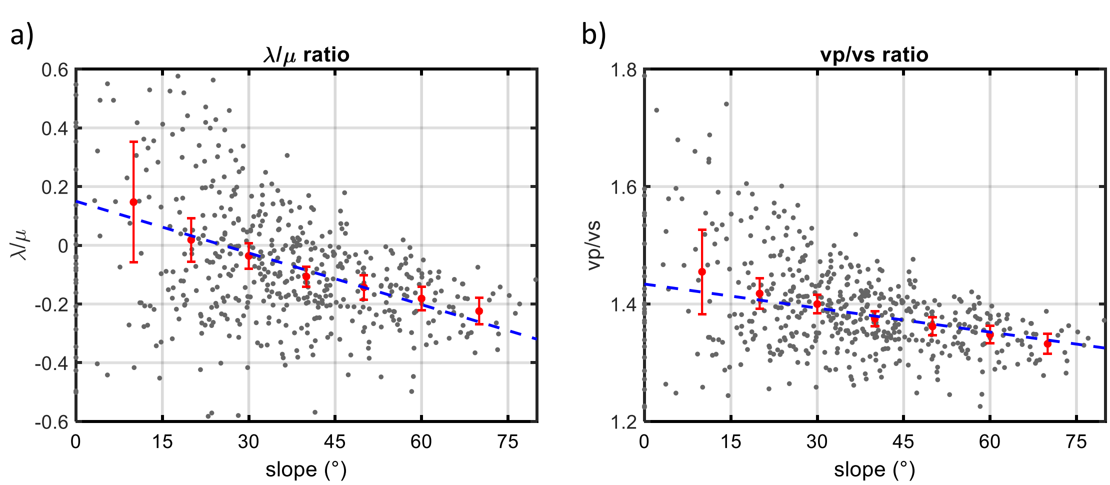

Fig. 6. The λ/μ ratio (a) and the v_P/v_S ratio (b) as a function of the slope angle. The black dots are the values for individual AEs, the red dots are the binned data, and the red lines are the 99% confidence intervals. The blue dashed line shows the linear regression. Note that the λ/μ ratio is negative for slopes greater than 20–25°.

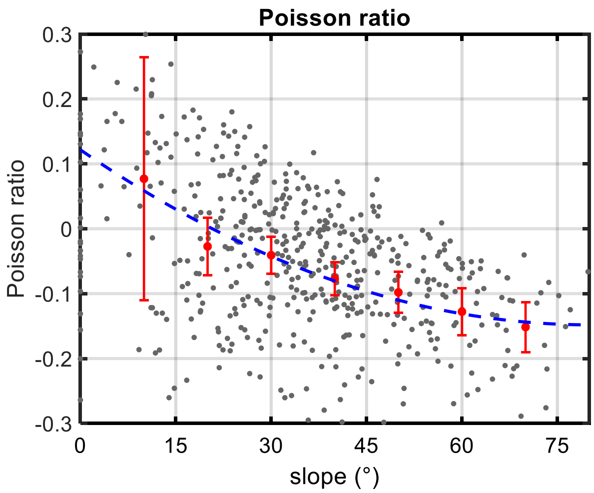

Fig. 7. The Poisson's ratio as a function of the slope angle. The black dots are the values for individual AEs, the red dots are the binned data, and the red lines are the 99% confidence intervals. The blue dashed line shows the quadratic regression. Note that the Poisson's ratio is negative for slopes greater than 20–25°.

The physical interpretation of the varying λ/μ ratio, v_P/v_S ratio, and Poisson's ratio is straightforward. The variation of the Poisson's ratio with increasing tensile character of fractures clearly indicates the bi-modularity of rocks, where the Poisson's ratio differs under tensile and compressive stress regimes.[27–32] Standard methods are capable of measuring the strength and the Poisson's ratio of rocks separately for two distinctly different stress modes: either for compressive or for tensile stress. They show that the strength and the Poisson's ratio are significantly lower under tensile stress than under compressive stress. Since our method measures rock properties for a mixed stress mode, it bridges the gap between these two distinct stress states. Consequently, the λ/μ ratio, v_P/v_S ratio, and the Poisson's ratio must vary, reflecting the gradual transition from the compressive to tensile stress regime.

Interestingly, as seen in Fig. 7, the Poisson's ratio ν becomes negative for slopes greater than 20–25°. Materials with the negative Poisson's ratio ν are called auxetic. Such materials are physically realizable, but their properties are rather extraordinary: their volume increases, when they are compressed.[56] However, the values of λ/μ, v_P/v_S and ν ratios cannot be arbitrarily low. Since real material should satisfy stability conditions, the following restrictions should apply

$$\frac{\lambda}{\mu} > -\frac{2}{3}, \quad \frac{v_P}{v_S} > \frac{4}{3}, \quad \nu > -1. \tag{15}$$

These limits are valid also for our binned data (Figs. 6 and 7, blue dashed lines).

Theoretical models of the effects of porosity, pore/crack geometry and fluid content on the Poisson's ratio are reviewed by Lutz and Zimmerman.[57] The authors also discuss theoretical models of auxetic porous materials. Concerning real rocks, the conditions for their auxetic behaviour have been studied in the lab by many authors.[58–62] A negative Poisson's ratio was observed, e.g., in sandstone and siltstone, primarily due to the low Poisson's ratio of quartz.[61] Other factors contributing to the reduction of the Poison's ratio in these rocks include high porosity, high crack density, high clay content, low pressure, and high temperature. In particular, the negative Poisson's ratio is often associated with rocks displaying high porosity and a high density of microcracks.[60] With increasing pressure, the microcracks and pores within the rock samples gradually close, and the Poisson's ratio progressively increases and becomes positive. The auxetic behaviour of volcanic rocks (basalt and rhyolite samples) with extremely high porosity was also studied by Ji et al.[63] The authors found that auxetic behaviour cannot occur for water-saturated volcanic rocks but may appear in dry basalts.

Based on the mentioned experimental studies of porous/fractured rocks under compressive and tensile stress showing bi-modular[27–32] and auxetic[58–63] behaviour of rocks, we conclude that the presented AE approach might provide valuable and independent information on physical properties of porous/fractured rocks. Since AEs can display shear, compression and tension fracture modes, rock properties can be measured in dependence on the fracture character of cracks. This approach is unique, because it allows the variation of λ/μ, v_P/v_S, and Poisson's ratio, indicating the bi-modular behaviour of a rock, to be observed in the same rock sample during a single experiment.

6. Conclusion

By calculating accurate moment tensors of 539 AEs recorded during a semi-circular bend test, we determined the λ/μ, v_P/v_S, and Poisson's ratios of the Tesin sandstone from the Reka mine (Czech Republic). The ratios vary depending on the fracturing mode of AEs, which suggests a bi-modular nature of the rock. For highly tensile cracks characterized by the slope angle of 80–90°, the v_P/v_S, λ/μ, and Poisson's ratio are 1.3, −0.3 and −0.15, respectively. The negative value of the Poisson's ratio points to auxetic behaviour of the rock. With an increasing shear component in AEs, the v_P/v_S, λ/μ, and Poisson's ratio increase. Consequently, λ/μ and Poisson's ratio become positive and the auxetic effects disappear.

The proposed approach for determining the λ/μ, v_P/v_S, and Poisson's ratios using AEs is entirely independent of standard techniques based on measuring the deformation of rock samples.[29,32,64] It is capable of measuring rock properties for mixed stress modes and highlights the significance of AE experiments for understanding fracture processes in rocks. The approach may find applications, particularly, in detailed studies of rock behaviour under various stress conditions.

In this paper, we focused on explaining basic principles of this pioneering method and demonstrated its advantages using the semi-circular bend test on the Tesin sandstone. Clearly, the method requires more extensive validation to be adopted by the rock mechanics community. Therefore, its applicability to other tests and types of rocks are presented in the follow-up paper by Petružálek et al.[65]

Declaration of competing interest

The authors declare that they have no known competing financial interests or personal relationships that could have appeared to influence the work reported in this paper.

Data availability

Data are included in the Electronic Supplement

Acknowledgments

We thank Associate Editor and the two anonymous reviewers for their constructive and helpful reviews. The theoretical analysis, data processing and interpretations were supported by the Czech Science Foundation, grant No. 22-10747S. The development of the experimental device for data acquisition and rock sample measurements were financed by the Czech Science Foundation grant No. 22-00580S and by the Czech Academy of Sciences project RVO 67985831.

Appendix A. Supplementary data

Supplementary data to this article can be found online at https://doi.org/10.1016/j.ijrmms.2023.105576.

References

1 Knopoff L, Randall MJ. The compensated linear vector dipole: a possible mechanism for deep earthquakes. *J Geophys Res*. 1970;75:4957–4963.
2 Jost ML, Hermann RB. A student's guide to and review of moment tensors. *Seismol Res Lett*. 1989;60:37–57.
3 Vavryčuk V. Moment tensor decompositions revisited. *J Seismol*. 2015;19(1): 231–252. https://doi.org/10.1007/s10950-014-9463-y.
4 Rudajev V, Šílený J. Seismic events with non-shear components, II, Rockbursts with implosive source component. *Pure Appl Geophys*. 1985;123:17–25.
5 Mori J, McKee C. Outward-dipping ring-fault structure at Rabaul caldera as shown by earthquake locations. *Science*. 1987;235:193–195.
6 Feigneir B, Young RP. Moment tensor inversion of induced microseismic events: evidence of non-shear failures in the −4< M <−2 moment magnitude range. *Geophys Res Lett*. 1992;19:1503–1506.
7 Julian BR, Miller AD, Foulger GR. Non-double-couple earthquakes 1: theory. *Rev Geophys*. 1998;36:525–549.
8 Miller AD, Foulger GR, Julian BR. Non-double-couple earthquakes 2: observations. *Rev Geophys*. 1998;36:551–568.
9 Šílený J, Milev A. Source mechanism of mining induced seismic events—resolution of double couple and non double couple models. *Tectonophysics*. 2008;456(1–2):3–15. https://doi.org/10.1016/j.tecto.2006.09.021.
10 Vavryčuk V. Focal mechanisms in anisotropic media. *Geophys J Int*. 2005;161: 334–346. https://doi.org/10.1111/j.1365-246X.2005.02585.x.
11 Vavryčuk V. Spatially dependent seismic anisotropy in the Tonga subduction zone: a possible contributor to the complexity of deep earthquakes. *Phys Earth Planet In*. 2006;155:63–72. https://doi.org/10.1016/j.pepi.2005.10.005.
12 Vavryčuk V, Bohnhoff M, Jechumtálová Z, Kolář P, Šílený J. Non-double-couple mechanisms of micro-earthquakes induced during the 2000 injection experiment at the KTB site, Germany: a result of tensile faulting or anisotropy of a rock? *Tectonophysics*. 2008;456:74–93. https://doi.org/10.1016/j.tecto.2007.08.019.
13 Vavryčuk V. Inversion for parameters of tensile earthquakes. *J Geophys Res*. 2001; 106(B8):16339–16355. https://doi.org/10.1029/2001JB000372.
14 Vavryčuk V. Tensile earthquakes: theory, modeling, and inversion. *J Geophys Res*. 2011;116(B12), B12320. https://doi.org/10.1029/2011JB008770.
15 Šílený J. Resolution of non-double-couple mechanisms: simulation of hypocenter mislocation and velocity structure mismodeling. *Bull Seismol Soc Am*. 2009;99(4): 2265–2272. https://doi.org/10.1785/0120080335.
16 Vavryčuk V, Hrubcová P. Seismological evidence of fault weakening due to erosion by fluids from observations of intraplate earthquake swarms. *J Geophys Res Solid Earth*. 2017;122(5):3701–3718. https://doi.org/10.1002/2017JB013958.
17 Petružálek M, Jechumtálová Z, Kolář P, et al. Acoustic emission in a laboratory: mechanism of microearthquakes using alternative source models. *J Geophys Res Solid Earth*. 2018;123(6):4965–4982. https://doi.org/10.1029/2017JB015393.
18 Petružálek M, Jechumtálová Z, Šílený J, Kolář P, Svitek T, Lokajíček T. Turková I, Kotrly M, Onysko R. Application of the shear-tensile source model to acoustic emissions in Westerly granite. *Int J Rock Mech Min Sci*. 2020;128, 104246. https://doi.org/10.1016/j.ijrmms.2020.104246.
19 Vavryčuk V, Adamová P, Doubravová J, Ren Y. Mapping stress and fluids on faults by nonshear earthquakes. *J Geophys Res Solid Earth*. 2021;126, e2020JB021287. https://doi.org/10.1029/2020JB021287.
20 Ross AG, Foulger GR, Julian BR. Non-double-couple earthquake mechanisms at the Geysers geothermal area, California. *Geophys Res Lett*. 1996;23:877–880.
21 Julian BR, Miller AD, Foulger GR. Non-double-couple earthquake mechanisms at the Hengill–Grensdalur volcanic complex, southwest Iceland. *Geophys Res Lett*. 1997;24: 743–746.
22 Sarao A, Cocina O, Privitera E, Panza GF. The dynamics of the 2001 Etna eruption as seen by full moment tensor analysis. *Geophys J Int*. 2010;181:951–965.
23 Ren Y, Vavryčuk V, Wu S, Gao Y. Accurate moment tensor inversion of acoustic emissions and its application to Brazilian splitting test. *Int J Rock Mech Min Sci*. 2021; 141, 104707. https://doi.org/10.1016/j.ijrmms.2021.104707.
24 Dalguer LA, Irikura K, Dieta JD. Simulation of tensile crack generation by three-dimensional dynamic shear rupture propagation during an earthquake. *J Geophys Res*. 2003;108(B3):2144. https://doi.org/10.1029/2001JB001738.
25 Griffith WA, Rosakis A, Pollard DD, Ko CW. Dynamic rupture experiments elucidate tensile crack development during propagating earthquake ruptures. *Geology*. 2009; 37:795–798. https://doi.org/10.1130/G30064A.1.
26 Misra S, Mandal N, Dhar R, Chakraborty C. Mechanisms of deformation localization at the tips of shear fractures: findings from analogue experiments and field evidence. *J Geophys Res*. 2009;114, B04204. https://doi.org/10.1029/2008JB005737.
27 Stimpson B, Chen R. Measurement of rock elastic moduli in tension and in compression and its practical significance. *Can Geotech J*. 1993;30:338–347.
28 Yu X, da Gama CD, Na Y, Wang Q, Xie Q. Deformation behaviour of rocks under compression and direct tension. *J S Afr Inst Min Metall*. 2005;105(1):55–62.
29 Patel S, Martin CD. Evaluation of tensile Young's modulus and Poisson's ratio of a bi-modular rock from the displacement measurements in a Brazilian test. *Rock Mech Rock Eng*. 2018;51:361–373. https://doi.org/10.1007/s00603-017-1345-5.
30 Zhu JB, Zhou T, Liao ZY, Sun L, Li XB, Chen R. Replication of internal defects and investigation of mechanical and fracture behaviour of rock using 3D printing and 3D numerical methods in combination with X-ray computerized tomography. *Int J Rock Mech Min Sci*. 2018;106:198–212. https://doi.org/10.1016/j.ijrmms.2018.04.022.
31 Li D, Li B, Han Z, Zhu Q, Liu M. Evaluation of bi-modular behavior of rocks subjected to uniaxial compression and Brazilian tensile testing. *Rock Mech Rock Eng*. 2021;54: 3961–3975. https://doi.org/10.1007/s00603-021-02469-0.
32 Misa R, Nowakowski A. Comparison of the compressive and tensile strength values of rocks obtained on the basis of various standards and recommendations. *Symmetry*. 2021;13:1163. https://doi.org/10.3390/sym13071163.
33 Li L, Ji S. A new interpretation for formation of orthogonal joints in quartz sandstone. *J Rock Mech Geotech Eng*. 2021;13:289–299. https://doi.org/10.1016/j.jrmge.2020.08.003.
34 Aki K, Richards PG. *Quantitative Seismology, Theory and Methods*. San Francisco: W.H. Freeman; 1980.
35 Lay T, Wallace TC. *Modern Global Seismology*. New York, NY: Academic Press; 1995.
36 Kuruppu MD, Obara Y, Ayatollahi MR, Chong KP, Funatsu T. ISRM-suggested method for determining the mode I static fracture toughness using semi-circular bend specimen. *Rock Mech Rock Eng*. 2014;47(1):267–274.
37 Chong KP, Kuruppu MD, Kuszmaul JS. Fracture toughness determination of layered materials. *Eng Fract Mech*. 1987;28(1):43–54.
38 Aminzadeh A, Fahimifar A, Nejati M. On Brazilian disk test for mixed-mode I/II fracture toughness experiments of anisotropic rocks. *Theor Appl Fract Mech*. 2019; 102:222–238.
39 Nejati M, Aminzadeh A, Saar MO, Driesner T. Modified semi-circular bend test to determine the fracture toughness of anisotropic rocks. *Eng Fract Mech*. 2019;213: 153–171.
40 Nejati M, Aminzadeh A, Driesner T, Saar MO. On the directional dependency of mode I fracture toughness in anisotropic rocks. *Theor Appl Fract Mech*. 2020;107, 102494.
41 Sedlak P, Hirose Y, Khan SA, Enoki M, Sikula J. New automatic localization technique of acoustic emission signals in thin metal plates. *Ultrasonics*. 2009;49(2): 254–262.
42 Petružálek M, Lokajíček T, Svitek T, Jechumtálová Z, Kolář P, Šílený J. Fracturing of migmatite monitored by acoustic emission and ultrasonic sounding. *Rock Mech Rock Eng*. 2019;52(1):47–59.
43 Davi R, Vavryčuk V. Seismic network calibration for retrieving accurate moment tensors. *Bull Seismol Soc Am*. 2012;102(6):2491–2506. https://doi.org/10.1785/0120110344.
44 Davi R, Vavryčuk V, Charalampidou E-M, Kwiatek G. Network sensor calibration for retrieving accurate moment tensors of acoustic emissions. *Int J Rock Mech Min Sci*. 2013;62:59–67. https://doi.org/10.1016/j.ijrmms.2013.04.004.
45 Lin Q, Yuan H, Biolzi L, Labuz JF. Opening and mixed mode fracture processes in a quasi-brittle material via digital imaging. *Eng Fract Mech*. 2014;131:176–193. https://doi.org/10.1016/j.engfracmech.2014.07.028.
46 Stierle E, Vavryčuk V, Šílený J, Bohnhoff M. Resolution of non-double-couple components in the seismic moment tensor using regional networks: 1. A synthetic case study. *Geophys J Int*. 2014;196(3):1869–1877. https://doi.org/10.1093/gji/ggt502.
47 Sokos E, Zahradník J. Isola — a Fortran code and Matlab GUI to perform multiple point source inversion of seismic data. *Comput Geosci*. 2008;34:967–977.
48 Cesca S, Dahm T. A frequency domain inversion code to retrieve time-dependent parameters of very long period volcanic sources. *Comput Geosci*. 2008;34(3): 235–246.
49 Fojtíková L, Vavryčuk V, Cipciar A, Madarás J. Focal mechanisms of micro-earthquakes in the dobrá voda seismoactive area in the malé karpaty mts. (little carpathians), Slovakia. *Tectonophysics*. 2010;492:213–229. https://doi.org/10.1016/j.tecto.2010.06.007.
50 Vavryčuk V, Kühn D. Moment tensor inversion of waveforms: a two-step time-frequency approach. *Geophys J Int*. 2012;190:1761–1776. https://doi.org/10.1111/j.1365-246X.2012.05592.x.
51 Šílený J, Vavryčuk V. Approximate retrieval of the point source in anisotropic media: numerical modelling by indirect parametrization of the source. *Geophys J Int*. 2000; 143:700–708. https://doi.org/10.1046/j.1365-246X.2000.00256.x.
52 Šílený J, Vavryčuk V. Can unbiased source be retrieved from anisotropic waveforms by using an isotropic model of the medium? *Tectonophysics*. 2002;356:125–138. https://doi.org/10.1016/S0040-1951(02)00380-3.
53 Vavryčuk V. Elastodynamic and elastostatic Green tensors for homogeneous weak transversely isotropic media. *Geophys J Int*. 1997;130(3):786–800. https://doi.org/10.1111/j.1365-246X.1997.tb01873.x.
54 Stierle E, Vavryčuk V, Kwiatek G, Charalampidou E-M, Bohnhoff M. Seismic moment tensors of acoustic emissions recorded during laboratory rock deformation experiments: sensitivity to attenuation and anisotropy. *Geophys J Int*. 2016;205(1): 38–50. https://doi.org/10.1093/gji/ggw009.
55 Aker E, Kühn D, Vavryčuk V, Soldal M, Oye V. Experimental investigation of acoustic emission and their moment tensors in rock during failure. *Int J Rock Mech Min Sci*. 2014;70:286–295. https://doi.org/10.1016/j.ijrmms.2014.05.003.
56 Evans KE, Alderson A. Auxetic materials: functional materials and structures from lateral thinking. *Adv Mater*. 2000;12(9):617–628.

57 Lutz MP, Zimmerman RW. The effect of pore shape on the Posson ratio of porous materials. *Math Mech Solid*. 2021;26(8):1191–1203. https://doi.org/10.1177/10812865211023535.
58 Dunn ML, Ledbetter H. Poisson's ratio of porous and microcracked solids: theory and application to oxide superconductors. *J Mater Res*. 1995;10(11):2715–2722.
59 Mainprice D, Le Page Y, Rodgers J, Jouanna P. Ab initio elastic properties of talc from 0 to 12 GPa: interpretation of seismic velocities at mantle pressures and prediction of auxetic behaviour at low pressure. *Earth Planet Sci Lett*. 2008;274: 327–338. https://doi.org/10.1016/j.epsl.2008.07.047.
60 Yu Ch, Ji S, Li Q. Effects of porosity on seismic velocities, elastic moduli and Poisson's ratios of solid materials and rocks. *J Rock Mech Geotech Eng*. 2016;8:35–49.
61 Ji S, Li L, Motra HB, et al. Poisson's ratio and auxetic properties of natural rocks. *J Geophys Res Solid Earth*. 2018;123:1161–1185. https://doi.org/10.1002/2017JB014606.
62 Zhao Z, Xu H, Wang J, Zhao X, Cai M, Yang Q. Auxetic behavior of Beishan granite after thermal treatment: a microcracking perspective. *Eng Fract Mech*. 2020;231, 107017. https://doi.org/10.1016/j.engfracmech.2020.107017.
63 Ji S, Wang Q, Li L. Seismic velocities, Poisson's ratios and potential auxetic behavior of volcanic rocks. *Tectonophysics*. 2019;766:270–282. https://doi.org/10.1016/j.tecto.2019.06.013.
64 Perras MA, Diederichs MS. A review of the tensile strength of rock: concepts and testing. *Geotech Geol Eng*. 2014;32:525–546. https://doi.org/10.1007/s10706-014-9732-0.
65 Petružálek M, Jechumtálová Z, Lokajíček T, Kolář P, Šílený J. Micro-fracturing in granitic rocks during uniaxial loading: the role of grain size heterogeneity. *Rock Mech Rock Eng*. 2023. submitted.